

Resistive pressure gradient-driven turbulence at stellarator plasma edge

L. Garcia

Universidad Carlos III, Madrid, Spain

B. A. Carreras, V. E. Lynch, J. N. Leboeuf, and D. E. Newman

Oak Ridge National Laboratory, Oak Ridge, Tennessee 37830

(Received 25 February 1997; accepted 4 June 1997)

High resolution calculations of resistive pressure gradient-driven turbulence for the plasma edge parameters of the Advanced Toroidal Facility (ATF) [J. F. Lyon *et al.*, *Fusion Technol.* **10**, 179 (1986)] electron cyclotron heated discharges give fluctuation levels, consistent with the experimental measurements. This turbulence model is also used to simulate the transition from the low confinement to the high confinement mode. The transition is triggered through the poloidal flow amplification induced by the Reynolds stress. After the transition, the confinement improvement is relatively low (30%–40%), even for unrealistically low poloidal viscosity. In the high confinement mode, the characteristic radial scale length of the poloidal flow in the three-dimensional calculations (separation between the lowest- n resonant surfaces) is different from the single helicity results (radial correlation length of the fluctuations). The simple criterion based on the ratio of shearing rate to the linear growth rate does not quantitatively account for the fluctuation reduction. © 1997 American Institute of Physics. [S1070-664X(97)02209-X]

I. INTRODUCTION

In stellarators, the transition from the low-confinement mode (L mode) to the high-confinement mode (H mode) has been less effective than in tokamaks. The confinement improvement in the H mode is only 30% higher than in the L mode.^{1,2} There are many possible reasons for that. It has been argued that in stellarators (1) the neoclassical viscosity is higher and does not allow the $E \times B$ flow shear to develop; (2) the ratio of the anomalous transport to neoclassical transport is lower, and as a result less improvement can be expected; and (3) the power density in present experiments is lower, and it has not yet been possible to explore the full capabilities of stellarator confinement. It is also possible that the Reynolds stress is less effective in amplifying the edge poloidal flow shear.^{3,4} The identification of the main cause for this lower performance can give a useful insight in the understanding of transition mechanisms and is essential in designing a more effective stellarator. The larger viscosity implies a larger power requirement to produce the same amount of flow amplification. However, if the Reynolds stress fails in amplifying the shear flow, there is no simple solution to a more effective H mode. Detailed modeling of the transition is necessary in the determination of the source of the problem.

To model the plasma edge in stellarators, we need to identify the basic mechanism for the turbulence drive. Many stellarator configurations are characterized by a magnetic hill at the edge.⁵ For these configurations, resistive interchange modes⁶ are likely unstable at the plasma edge and could be the dominant mechanism for edge plasma transport in those devices. There is some experimental evidence for this mechanism. Several analytical and numerical studies of resistive pressure–gradient-driven turbulence have been carried out.^{7–10} However, only analytical expressions without the inclusion of diamagnetic effects have been compared with experimental results. The analytically predicted resis-

tive interchange turbulence fluctuation levels were found to be consistent with the measured edge plasma fluctuation levels in the Advanced Toroidal Facility (ATF),^{11,12} but there have not been systematic comparisons between theory and experiment.

In recent years, the increase in computer capabilities has allowed high resolution turbulence calculations. In particular, the use of dedicated CRAY Y-MP C-90 time permitted their completion in a period of a few weeks. We have used this opportunity to carry out a resistive interchange turbulence calculation for the ATF plasma edge and compared the results with the fluctuation measurements.

We have used the same turbulence model to study a transition as a test of the Reynolds stress flow amplification in three-dimensional (3-D) resistive interchange turbulence. In this paper, we consider only electron cyclotron heated (ECH) discharges in ATF (no Ohmic heating). For these discharges, core ion temperatures are very low with $T_e/T_i \gg 1$. Although there are no ion temperature measurements at the edge, we assume that the inequality also holds at the edge. Therefore, ion diamagnetic effects have not been included. In the transition studies, only the shear poloidal velocity, V'_θ , contributes to the shear $E \times B$ flow turbulence suppression. This allows us to study the shear poloidal flow amplification and its characteristic radial scale in a 3-D turbulence calculation. After the transition, the confinement improvement is relatively low (30%–40%), even in the limit of negligible viscosity. The turbulent viscosity component of the Reynolds stress quickly overcomes its flow-destabilizing component. As a result, the level of shear amplification flow is too low for a full suppression of the turbulence.

The radial scale length of the electric field shear is an important issue because it can set the width of the edge temperature pedestal. In the H mode, it has been found that the characteristic radial scale length of the poloidal flow in the 3-D calculations is different from the single helicity results (2-D). In the latter case, the basic scale length of the flow is

the radial correlation length of the fluctuations, while for the H-mode solution the basic scale is the separation between the lowest- n resonant surfaces.

The rest of the paper is organized as follows. In Sec. II, the turbulence model is defined and the equilibrium conditions, together with linear stability results, are summarized in Sec. III. The numerical results for the L-mode regime are presented in Sec. IV, together with a comparison of the experimental measurements. In Sec. V, the transition dynamics and the turbulence properties in the H-mode state are discussed. Finally, the conclusions of this paper are presented in Sec. VI.

II. RESISTIVE PRESSURE GRADIENT-DRIVEN TURBULENCE EQUATIONS

Resistive interchange modes extend uniformly along the magnetic field lines. They are flute-like instabilities. Therefore, for these instabilities it is possible to average over the toroidal magnetic field modulation induced by the helical windings. Using the Greene and Johnson formalism¹³ and assuming a straight helical system, the averaged equilibrium magnetic field geometry has cylindrical symmetry. In this system, the magnetic field line curvature is given by the averaged magnetic field line curvature,

$$\kappa = \frac{\bar{r}}{R_0} B_0^2 V'' , \quad (1)$$

where a prime indicates the derivative with respect to the toroidal flux and $V' = \int dl/B$ is the specific volume enclosed by a flux surface. In Eq. (1), R_0 is the major radius of the stellarator, \bar{r} the averaged minor radius of a flux surface, and B_0 the toroidal magnetic field value at the magnetic axis.

The equations used to describe the stellarator plasma edge turbulence are the reduced equations used to study the resistive pressure gradient-driven instability.⁷ Here we use the same conventions and notations as in Ref. 7. The geometry is cylindrical with minor radius a and length $L_0 = 2\pi R_0$. We use the cylindrical coordinates r , θ , and z . In the electrostatic approximation, the resistive pressure gradient-driven turbulence model can be described by the perpendicular momentum balance equation:

$$\begin{aligned} \frac{\rho_m}{B_0} \frac{\partial \tilde{U}}{\partial t} = & -\frac{\rho_m}{B_0} \mathbf{V}_\perp \cdot \nabla \tilde{U} - \frac{1}{\eta B_0} \nabla_\parallel^2 \left(\tilde{\Phi} + \frac{T_{\text{eq}}}{|e|n_{\text{eq}}} \tilde{n} \right) \\ & + \kappa T_{\text{eq}} \frac{1}{r} \frac{\partial \tilde{n}}{\partial \theta} + \frac{\rho_m}{B_0} \mu_{1\perp} \nabla_\perp^2 \tilde{U}; \end{aligned} \quad (2)$$

the equation of state,

$$\begin{aligned} \frac{\partial \tilde{n}}{\partial t} = & -\tilde{\mathbf{V}}_\perp \cdot \nabla \tilde{n} - \frac{dn_{\text{eq}}}{dr} \tilde{V}_r + \frac{1}{\eta |e| B_0^2} \nabla_\parallel^2 \left(\tilde{\Phi} + \frac{T_{\text{eq}}}{|e|n_{\text{eq}}} \tilde{n} \right) \\ & + D_\perp \nabla_\perp^2 \tilde{n} + D_\parallel \nabla_\parallel^2 \tilde{n} - n_{\text{eq}} \nabla_\parallel \tilde{V}_\parallel; \end{aligned} \quad (3)$$

and the parallel momentum balance equation,

$$\begin{aligned} \frac{\partial \tilde{V}_\parallel}{\partial t} = & -\tilde{\mathbf{V}}_\perp \cdot \nabla \tilde{V}_\parallel - \tilde{V}_\parallel \nabla_\parallel \tilde{V}_\parallel - \frac{T_{\text{eq}}}{\rho_m} \nabla_\parallel \tilde{n} + \mu_{2\perp} \nabla_\perp^2 \tilde{V}_\parallel \\ & + \mu_\parallel \nabla_\parallel^2 \tilde{V}_\parallel. \end{aligned} \quad (4)$$

Here, n is the density, \mathbf{V}_\perp is the perpendicular velocity, U is the z component of the vorticity, V_\parallel is the parallel flow velocity, η is the resistivity, and ρ_m is the mass density. Because of the high electron parallel conduction, we neglect the electron temperature fluctuations, $\nabla_\parallel \tilde{T}_e = 0$. In Eqs. (2)–(4), T_{eq} is the equilibrium electron temperature profile that is not dynamically evolved. Electron diamagnetic terms have been included in these equations.³ The total magnetic field can be expressed in terms of the equilibrium poloidal flux function, Ψ_{eq} , as

$$\mathbf{B} = -(\nabla \Psi_{\text{eq}} \times \hat{z})/R_0 + B_0 \hat{z}. \quad (5)$$

The perpendicular velocity can be expressed in terms of a stream function $\tilde{\Phi}/B_0$,

$$\mathbf{V}_\perp = (\nabla \tilde{\Phi} \times \hat{z})/B_0. \quad (6)$$

Here, \hat{z} is the unit vector in the toroidal direction. The velocity streamfunction $\tilde{\Phi}/B_0$ is trivially related to the electrostatic potential $-\tilde{\Phi}$. The z component of the vorticity can be expressed in terms of the velocity streamfunction by $\tilde{U} = \nabla_\perp^2 \tilde{\Phi}$. The derivative parallel to the magnetic field, ∇_\parallel , is defined as $\nabla_\parallel f = \mathbf{B} \cdot \nabla f$.

In Eqs. (2), (3), and (4), an overtilde identifies perturbed quantities, and the subscript eq identifies equilibrium quantities. Each equation has a perpendicular dissipation term, with the characteristic coefficients D_\perp (the collisional cross-field particle transport), $\mu_{1\perp}$ (the collisional viscosity for the perpendicular flow), and $\mu_{2\perp}$ (the collisional viscosity for the parallel flow). Parallel transport coefficients have also been included in the parallel velocity and density equations. They are the parallel viscosity μ_\parallel and parallel density transport due to the coupling to sound waves, D_\parallel . Because the ion temperature is very low at the edge of the ECH-heated discharges, the parallel viscosity is assumed to be classical, that is $\mu_\parallel = 1.28 V_i^2 \tau_i$, where V_i is the ion thermal velocity and τ_i the ion-ion collision time. Some calculations have been done with only two equations, Eqs. (2) and (3), and the parallel velocity has been neglected. In this case, we use D_\parallel different from zero to simulate the coupling of the sound waves, otherwise this coefficient is zero.

The driving term of the resistive interchange instability is the pressure gradient in the bad curvature region ($\kappa > 0$). That is, these modes are unstable when $-\kappa (dn_{\text{eq}}/dr) > 0$. The second term on the right-hand side (rhs) of Eq. (2) is the field line bending term, which is stabilizing. The resistivity weakens this term and allows the instability to grow.

To study the coupling between the turbulence and global flows, we need the poloidal flow profile evolution equation. It is derived by taking the flux surface average of the poloidal momentum balance equation. The resulting equation gives the conservation of momentum:

$$\frac{\partial \langle V_\theta \rangle}{\partial t} = -\frac{1}{r^2} \frac{\partial}{\partial r} (r^2 \langle \tilde{V}_r \tilde{V}_\theta \rangle) - \hat{\mu} \langle V_\theta \rangle = \langle \tilde{V}_r \tilde{U} \rangle - \hat{\mu} \langle V_\theta \rangle. \quad (7)$$

Here, the angular brackets, $\langle \rangle$, indicate the poloidal and the toroidal angle average over a magnetic flux surface, and $\hat{\mu}$ is the collisional poloidal flow damping rate. The nonlinear convection terms in the poloidal momentum balance gener-

ate the nondiagonal $r\theta$ terms of the Reynolds stress tensor, which can be interpreted as a turbulent vorticity flux in Eq. (7). Due to the electrostatic approximation, there is no contribution to the Reynolds stress from the correlation of magnetic field perturbations.

For a torsatron like ATF, the high toroidal ripple introduces strong damping of the toroidal velocity. For values of the poloidal Mach number, $M_p = -E_r/(B_\theta V_i)$, of the order of 1 or less, the poloidal flow damping term is comparable to the equivalent tokamak term.¹⁴ Therefore, of the three possible contributions to the radial electric field derived from the averaged radial force balance,

$$-\frac{E_r}{B} = V_\theta - \frac{B_\theta}{B} V_\phi - \frac{1}{Z_i e n_i B} \frac{\partial p_i}{\partial r}, \quad (8)$$

only the poloidal ion flow can effectively contribute in the ECH discharges. A possible important contribution to the electric field shear in ECH stellarator plasmas is the jump between the electron and ion roots.¹⁵ This contribution can be very important at the plasma core for formation of internal transport barriers. However, it is possibly irrelevant at the plasma edge due to the high collisionality of these plasmas.

In the nonlinear instability studies, we also include the evolution of the averaged density and temperature gradients. The corresponding equations are

$$\frac{\partial \langle n \rangle}{\partial t} = -\frac{\partial}{\partial r} \langle \tilde{V}_r \tilde{n} \rangle + D_{0\perp} \frac{1}{r} \frac{\partial}{\partial r} \left(r \frac{\partial \langle n \rangle}{\partial r} \right). \quad (9)$$

Therefore, the complete set of equations used in the numerical calculations discussed here is Eqs. (2), (3), (4), (7), and (9). Note that the dissipation terms in the averaged poloidal flow and density equations are not necessarily the same as for the fluctuating quantities. The reason is that the dissipation terms in the fluctuation quantities are used to control the mode spectrum by making the dissipation terms mode dependent. In the case of the averaged poloidal velocity equation we use a drag term.

III. EQUILIBRIUM PARAMETERS AND LINEAR STABILITY

All calculations presented here are for ECH-heated plasma parameters of the outer one-third region of the ATF averaged radius. In the calculation, the radial variable (the averaged radius of the flux surface in the sense of Greene and Johnson¹³) has been normalized to $1.25\bar{a}_{\text{ATF}}$, where \bar{a}_{ATF} is the averaged ATF plasma radius. Hence, the region $0.6a < r < 0.8a$ in the calculations models the region $0.50\bar{a}_{\text{ATF}} < r < \bar{a}_{\text{ATF}}$ in ATF plasmas. We have limited the nonlinear calculation to this plasma region because of computational constraints. The averaged rotational transform and V' profiles have been calculated from the ATF vacuum magnetic fields.¹⁶ Plasma density and electron temperature profiles have been chosen to fit the experimental ones in this region. In Fig. 1, we have plotted the rotational transform, the averaged curvature, and the normalized electron density and temperature profiles used in the calculations. The density and temperature profiles are flat within $r=0.5a$, and the peak values correspond to the measured values at this loca-

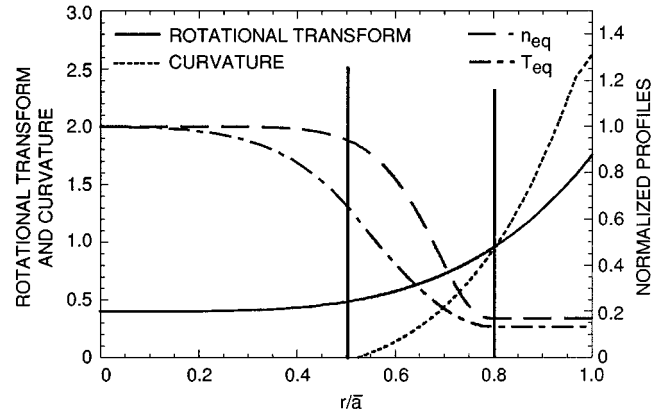


FIG. 1. Rotational transform, averaged curvature, the normalized density, and temperature profiles used in the calculations.

tion. In particular, the peak density, n_0 , is $4.2 \times 10^{12} \text{ cm}^{-3}$, and the peak electron temperature, T_{e0} , 300 eV. The magnetic field is 1 T and the Z_{eff} is assumed to be constant and equal to 2. For these values of the experimental parameters, the three dimensionless parameters relevant to the resistive interchange stability are $\beta_0/2\epsilon^2 = 0.010$, $\rho_s/a = 0.52 \times 10^{-2}$, and the Linquist number $S = 5 \times 10^5$. Here, $\beta_0 = T_{e0}n_0/(B^2/2)$ is the peak beta, $\epsilon = a/R$ is the inverse aspect ratio, and ρ_s is the sound Larmor radius. The averaged curvature is negative within $r=0.5a$, therefore, in this region the resistive interchange modes are stable.

The nonlinear calculations have been performed with the initial value code KITE.¹⁷ All quantities in Eqs. (2)–(4) are expressed in terms of a Fourier expansion in the angular variables of the form

$$f(r, \theta, \zeta, t) = \sum_{m,n} [f_{m,n}^s(r, t) \sin(m\theta + n\zeta) + f_{m,n}^c(r, t) \cos(m\theta + n\zeta)]. \quad (10)$$

The Fourier components are discretized using finite differences in the time and radial variables. The calculations have been done with a nonuniform radial grid of 420 points, with a radial resolution $\Delta r = 0.000665$ in the $0.6a < r < 0.8a$ region. Up to 4605 Fourier components have been included in the calculation. The maximum m value is about 110. Over 1000 rational surfaces are resolved. The radial distribution of the components included is shown in Fig. 2. These parameters represent a factor of 4 improvement on radial resolution and nearly a factor of 10 on the number of Fourier components from previous calculations.⁷

The coefficients of the perpendicular dissipation terms are assumed to be a function of m . The functional form is chosen to minimize the effect of the dissipation at low m and to sharply increase at high m . A convenient functional form for our particular distribution of modes is $\text{Tanh}[(m - 45)/15]$. At low m the coefficients of the dissipative terms are $D_\perp = \mu_{1\perp} = \mu_{2\perp} = 5 \times 10^{-3} a^2 / \tau_R$, and they are augmented by a factor of 100 in the high- m range. In this way, for $m < 45$, the linear growth rate of the main helicities is only weakly affected by the dissipation, but modes with $m > 45$ have a reduced growth rate and for $m > 60$ they are

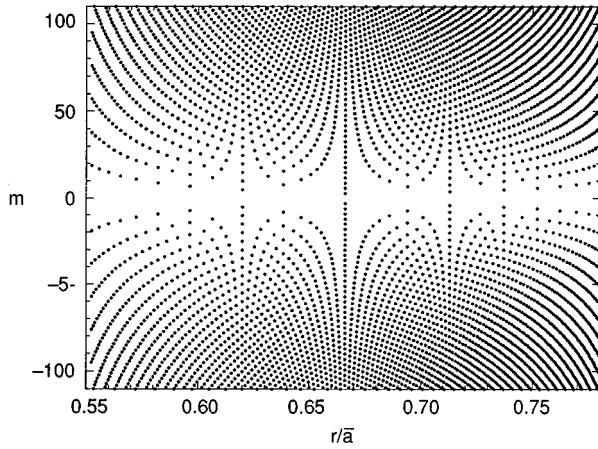


FIG. 2. The radial distribution of the Fourier components included in the nonlinear calculations.

linearly stabilized (Fig. 3). We have a significant range of stable modes ($60 < m < 110$). The value for the dissipation terms is lower than any other calculation we have done for resistive interchange turbulence. With this viscosity level, the Reynolds number is about 3×10^4 .

Most of the diagnostics used in these calculations are based on flux surface averages of quadratic quantities, such as the rms value of the fluctuation levels and the particle flux. In terms of the expansion given in Eq. (9), they have the generic form

$$\langle \tilde{f} \tilde{g} \rangle = \frac{1}{2} \sum_{m,n} (f_{m,n}^s g_{m,n}^s + f_{m,n}^c g_{m,n}^c). \quad (11)$$

Because the dissipation is low (high Reynolds number), we test two different time stepping methods (second- and third-order accuracy in Δt), and monitor the step size for error control. The basic tests are done for single helicity calculations to reduce the expense of the test. The second-order scheme is accurate enough. Convergence studies have been done by comparing two full 3-D nonlinear calculations with 2500 and 4605 Fourier components, respectively. Figure 4 shows the nonlinear evolution of the potential fluctuation at $r=0.66a$ for both calculations. Since both calculations

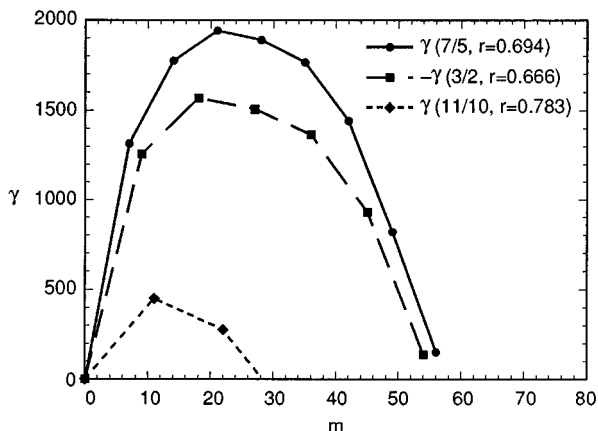


FIG. 3. Linear growth rate of the modes in three helicities included in the nonlinear calculations.

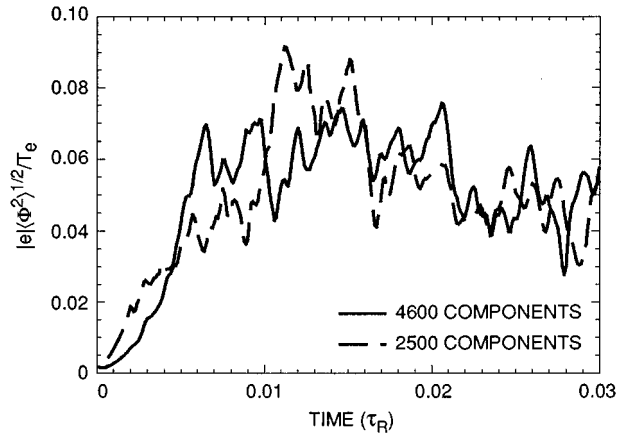


FIG. 4. Nonlinear evolution of the potential fluctuation at $r=0.66a$ for two full 3-D nonlinear calculations with 2500 and 4605 Fourier components, respectively.

were initialized with a random set of initial fluctuations, the initial phase of the calculations shows some differences. However, the time-averaged quantities over the nonlinear phase agree very well. This is also the case of the basic time scales. The largest size calculations were performed in parallel on the CRAY-MP C90 as part of the Special Parallel Processing (SPP) program at the National Energy Research Supercomputer Center (NERSC). The calculations have been made 98% parallel and an overlap of close to 14 processors is routinely achieved with aggregate speeds of about 5 Gflop/s.

IV. NONLINEAR NUMERICAL RESULTS

To begin the nonlinear calculations, we take a set of random fluctuations with averaged level of the order of 10^{-4} . That is, we use the expansion in Eq. (9) with Fourier components that are Gaussian functions of r . Each component peaks at the corresponding resonant surface r_s [$q(r_s) = m/n$] and each has an amplitude that is randomly determined to be between zero and 10^{-4} . The fastest growing modes dominate the initial phase of the calculation, in which the fluctuations grow at an approximately exponential rate.

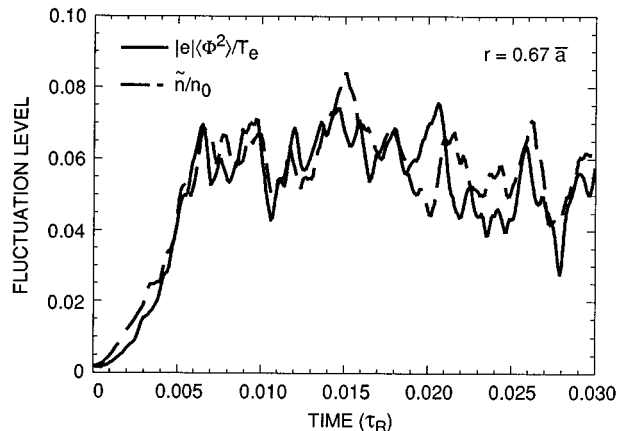


FIG. 5. Nonlinear evolution of the density and electrostatic potential fluctuations.

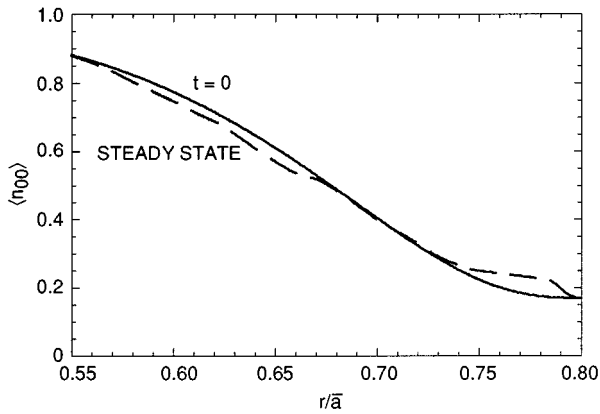


FIG. 6. The time-averaged density profile during the steady-state phase of the calculation compared to the initial density profile.

After this initial phase, the density and electrostatic potential fluctuations nonlinearly evolve to a saturated state (Fig. 5). The averaged density profile is slightly changed by the quasilinear effects, but maintains a nonzero gradient. At the main resonant surfaces, this change of the density profile causes a reduction of the linear growth rates by less than a factor of 2. Therefore, the nonlinear saturation is dominated by the transfer of energy to damped high- m modes, where it is dissipated. The time-averaged density profile during the steady-state phase of the calculation is shown in Fig. 6 and compared to the initial density profile.

To characterize the nonlinear turbulent state, the rms fluctuation levels have been time averaged over the steady-state phase. In Fig. 7, the rms electrostatic potential fluctuation level is shown. In the figure, the singular surfaces with $n < 8$ are indicated with vertical bars. The time-averaged fluctuation levels have profiles that increase toward the edge, reaching values close to 10%. They show radial structures that are correlated with the resonant surfaces of the lowest- n modes.¹⁸ A similar type of plot for the time-averaged poloidal flow is presented in Fig. 8. The averaged poloidal flow level remains small because we have used a large viscosity for the $m=0$; the $n=0$ component of the flow ($\hat{\mu}$

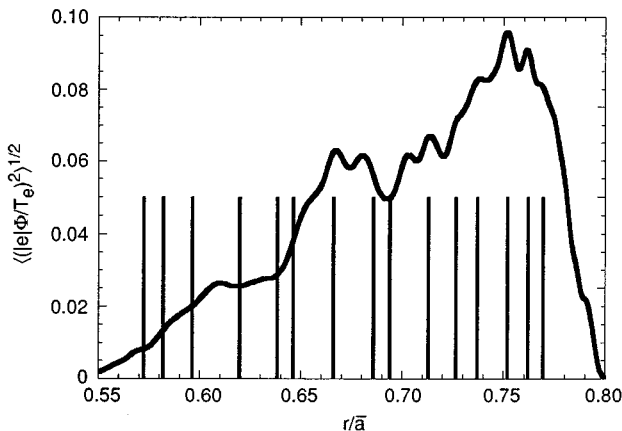


FIG. 7. Radial profile of the rms electrostatic potential fluctuation level, averaged over the steady-state phase of the calculation. The radial position of the singular surfaces with a lowest- n mode such as $n < 8$ are indicated with vertical bars.

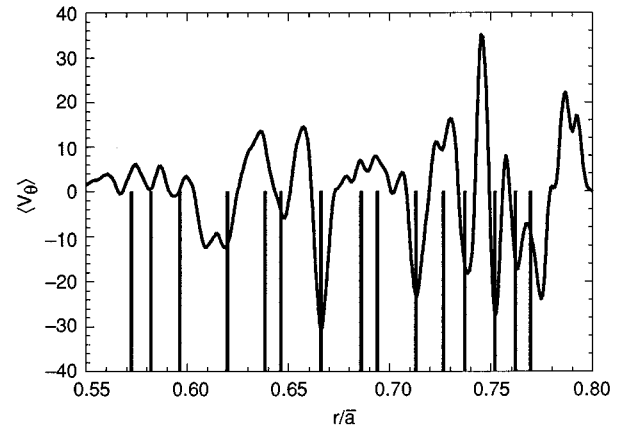


FIG. 8. The time-averaged poloidal flow profile. The radial position of the singular surfaces with a lowest- n mode such as $n < 8$ are indicated with vertical bars.

$= 10^4 a / \tau_R$). As was shown by single helicity calculations when diamagnetic effects are included,³ the flow generated through Reynolds stress has a minimum at the resonance surfaces. This structure seems to hold in the 3-D calculations, as is shown in Fig. 8. The radial scale of this flow structure is comparable to the radial correlation length of the fluctuations.

In the steady-state phase of the nonlinear evolution, to calculate the radial correlation length of the fluctuations, we first time average the coherence $\gamma(r, \Delta r, t)$ at different radial positions,

$$\gamma(r, \Delta r, t) \equiv \frac{\langle \tilde{f}(r, \theta, \zeta, t) \tilde{f}(r - \Delta r, \theta, \zeta, t) \rangle}{\langle \tilde{f}(r, \theta, \zeta, t)^2 \rangle}. \quad (12)$$

The radial correlation length, Δ_r , is the value of Δr corresponding to the e^{-1} value of the time-averaged coherence. As a function of the radial position, the radial correlation length shows some structure that is related to the low- m resonant surfaces. This is shown in Fig. 9, where we have plotted the radial correlation length of the electrostatic potential fluctuations. The density fluctuations correlation length has a similar radial dependence, although its value is about 12% larger. The correlation length at the position of

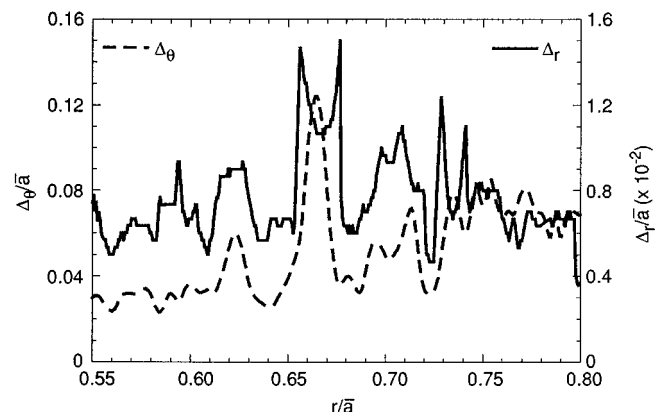


FIG. 9. Radial and poloidal correlation lengths of the potential fluctuations in the steady-state phase as a function of the radial position.

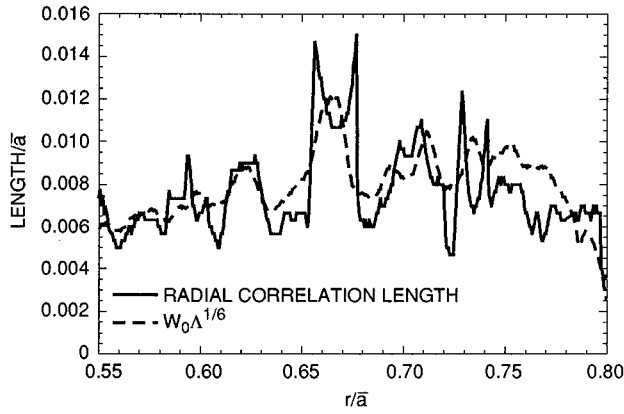


FIG. 10. Radial correlation length and renormalized mode width of the potential fluctuations as a function of the radial position.

the rational surfaces is close to the characteristic radial width of the linear eigenmodes, W . From Ref. 7, the renormalized width is given by $W \approx W_0 \Lambda^{1/6}$, where

$$W_0 = \left\{ \left[\frac{\beta_0}{2\epsilon^2} \kappa \frac{T_e(r)}{T_e(0)} \left(\frac{-a}{n_0(0)} \frac{dn_0}{dr} \right) \right]^{1/2} \times \frac{\eta(r)}{\eta(0)S} \frac{q^2 L_q^2}{mar} \right\}^{1/3} a \quad (13)$$

is the radial width of the linear eigenmode and Λ is the solution of the equation

$$\Lambda = \frac{2}{3\pi} \ln \left\{ \left[\frac{\beta_0}{2\epsilon^2} \kappa \frac{T_e(r)}{T_e(0)} \left(\frac{-a}{n_0(0)} \frac{dn_0}{dr} \right) \right]^{-1} \times \left(\frac{r}{am} \right)^4 128 \left(\frac{\eta(0)S}{\eta(r)} \right)^2 \right\} - \frac{2}{\pi} \ln \Lambda. \quad (14)$$

Here, $L_q = [(1/q)(dq/dr)]^{-1}$. In these expressions, we use as the density gradient the time-averaged gradient over the nonlinear phase of the calculation and for m the value of the spectral-averaged poloidal mode number that will be described later. In Fig. 10, we have plotted the renormalized width as a function of the radius and compared it with the radial correlation length. The radial width tracks closely the radial structures of the correlation length. The radial averaged value of the radial correlation length of the electrostatic potential fluctuations is $\Delta_r = 0.0076 \pm 0.004a$ and for the density fluctuations $\Delta_r = 0.0085 \pm 0.005a$. For ATF parameters, these values correspond to $\Delta_r = 0.26 \pm 0.13$ cm for the potential fluctuations and $\Delta_r = 0.27 \pm 0.17$ cm for the density fluctuations.

The time-averaged poloidal wave number spectrum peaks at the lowest values of m (Fig. 11). The power spectrum of both density and potential fluctuations has a power dependence for $m > 10$ with a decay index of -3.57 ± 0.03 . The main difference with the spectra calculated in Ref. 9 is for that case $\omega_* = 0$. In the present calculation, $\omega_* \neq 0$ and the decay indexes are practically the same for density and potential fluctuations. This is a consequence of the nearly adiabatic behavior of the fluctuations.

We can calculate the poloidal correlation length from the spectral-averaged poloidal mode number m ,

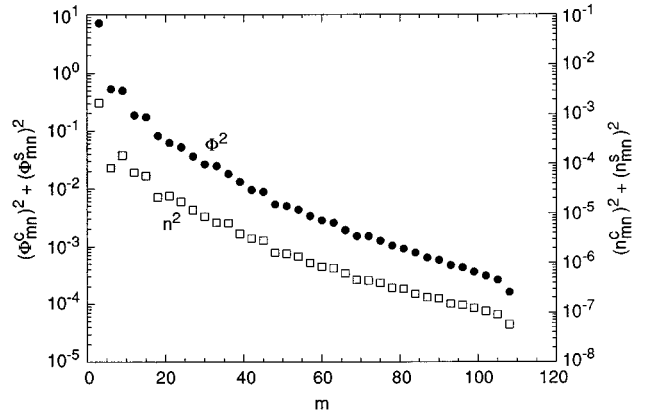


FIG. 11. Time-averaged poloidal wave number spectrum of the electrostatic potential and density fluctuations.

$$\{m^2\} \equiv \frac{\sum_{m,n} m^2 [(\Phi_{m,n}^s)^2 + (\Phi_{m,n}^c)^2]}{\sum_{m,n} [(\Phi_{m,n}^s)^2 + (\Phi_{m,n}^c)^2]}. \quad (15)$$

By time averaging $\{m^2\}$ over the steady-state phase of the calculation, we can evaluate the rms poloidal wave number $k_\theta \equiv \{m^2\}^{1/2}/\bar{r}$. For ATF edge parameters, its value varies between 0.5 and 1.0 cm^{-1} . Then, we define as the poloidal correlation length the inverse of the spectral-averaged k_θ , and its radial dependence is shown in Fig. 9. The radial-averaged poloidal correlation length is $\Delta_\theta = 0.05a$, about seven times the averaged radial correlation length. This value corresponds to 1.7 cm for ATF parameters.

The frequency spectrum for potential and density fluctuations are similar. They peak at low frequencies and decay as $\omega^{-2.2}$. We can calculate the decorrelation time, τ_c , using

$$\tau_c \approx \frac{2}{[(\omega^2 - [\omega]^2)]}, \quad (16)$$

where the square bracket indicates spectral averaging. The radial average of the potential fluctuation decorrelation time is $\tau_c \approx 1.6 \times 10^{-3} \tau_R^{-1}$.

To compare the results of the turbulence calculations with experimental fluctuation measurements, we use the ATF fluctuation data discussed in Ref. 11. The fluctuation data available includes the measurements by reflectometry¹¹ and edge Langmuir probes.¹⁹ The result of the comparison is shown in Fig. 12. There is reasonable agreement between the model and the experimental data. However, the experimental fluctuation profiles seem to fall off faster with the radius toward the inside. Note that the drive is cut off beyond $r/a_{\text{ATF}} = 0.98$ in the calculation. Beyond this radius, some other drive is needed to explain the large level of fluctuations.¹² Note that the averaged radius in Fig. 12 is normalized to \bar{a}_{ATF} instead of $a = 1.25\bar{a}_{\text{ATF}}$.

Having calculated the fluctuation amplitude and cross-correlation, it is possible to determine the effective diffusivity by dividing the particle flux by the density gradient. The result is shown in Fig. 13, together with the radial profile of the particle flux. The averaged diffusivity over the radial interval considered in these calculations is $D_{\text{eff}} = 0.075\bar{a}^2/\tau_R$. Since the decorrelation time of the turbulence is $\tau_c \approx 1.6 \times 10^{-3} \tau_R^{-1}$, the mixing length estimate for the dif-

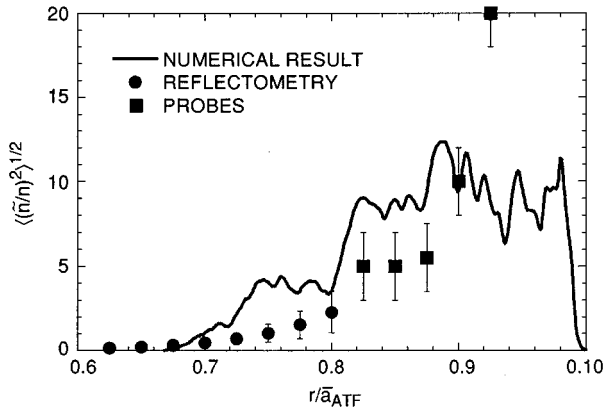


FIG. 12. A comparison between the results of the turbulence calculations with experimental fluctuation measurements in the ATF.¹¹

fusivity is $D \approx \Delta_r^2 \tau_c \approx 0.024 \bar{a}^2 / \tau_R$, which is about a factor of 3 below the calculated diffusivity. This factor is consistent with previous⁷ evaluations of the diffusivities using the mixing length approximation. This value corresponds to 0.1 m²/s, which is low compared with ATF confinement. The reason for the low value of the diffusivity is the near-adiabatic character of the fluctuations. The relative phase between the density fluctuations and the radial fluctuating flow, α_p , is also plotted in Fig. 13. The cosine of α_p stays around 0.2 over the whole radius.

V. TRANSITION TO A HIGH-CONFINEMENT REGIME

Since this edge turbulence model seems to reproduce some of the features of the ATF stellarator edge fluctuation and transport, it is interesting to use it to explore the properties of the L–H transition in stellarators. The short operation time of the ATF did not allow an H-mode discharge to be obtained. However, in recent years, stellarator configurations as disparate as Compact Helical Stellarator (CHS) and Wendelstein 7 Advanced Stellarator (W7-AS)²⁰ have succeeded in obtaining H-mode discharges. The properties of the H mode are similar in both devices. Therefore, we can assume that given adequate operation time, ATF would also have ob-

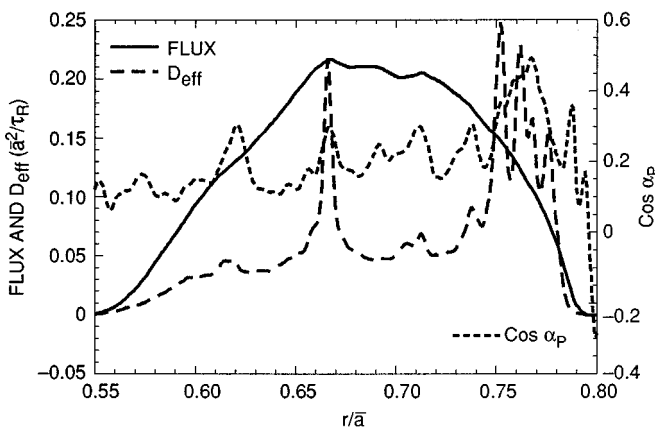


FIG. 13. Radial profile of the particle flux, the effective particle diffusivity, and the cosine of the relative phase between the density fluctuations and the radial fluctuating velocity.

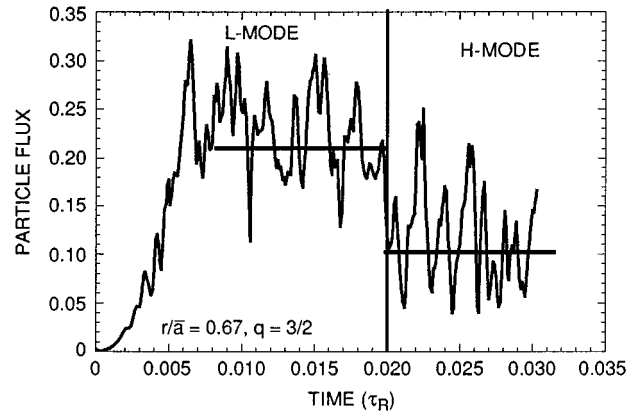


FIG. 14. Nonlinear evolution of the particle flux. At $t=0.0204\tau_R$, the transition from the L- to the H-mode state is triggered.

tained a similar H mode. Hence, using the present model, we can have some idea of what kind of change in confinement may be expected.

To do a realistic simulation of the L–H transition would require coupling this turbulence model to the evolution of averaged profiles, including particle and energy sources, varying the power source, and waiting for a spontaneous transition. That requires carrying out the calculation over a transport time scale. Such a long calculation is impossible with present computer capabilities for large-scale turbulence calculations like the ones described in this paper. For the resistive interchange model used in this paper, the simplest way of causing a transition is by reducing the viscous drag in the averaged poloidal flow equation, Eq. (8). Therefore, we use this approach to trigger a transition. Since we are interested in maximizing the effects on the confinement, we take down the viscosity by several orders of magnitude over all the radial extents of the calculation. The reason for reducing $\hat{\mu}$ over such a large radial region is to find out the natural length scale of the shear flow in the improved confinement mode and avoid the determination of the radial extent by the size of the region of low viscosity.

For the same calculation of Fig. 5, at $t=0.0204\tau_R$, we have reduced the averaged poloidal flow damping from $\hat{\mu} = 10^4 \tau_R^{-1}$ to $\hat{\mu} = 10^{-4} \tau_R^{-1}$. The transition occurs very shortly after the change in $\hat{\mu}$, after $7 \times 10^{-4} \tau_R$, that is about 100 μ s for ATF parameters. If we plot the evolution of the particle flux with time at a fixed radial position, the transition is clearly identified (Fig. 14). In Fig. 14, the time-averaged flux over the H-mode phase is about a factor of 2 lower than the flux in the L-mode phase. The reduction of the flux starts at the edge but very quickly extends over most of the radial region (Fig. 15). The reduction shown in Fig. 14 is somewhat misleading because the plot is at a fixed radius and there is not the same level of reduction at all radial positions. Taking the radial average of the flux, the reduction is only about 27%. The main cause of the flux reduction is fluctuation reduction (Fig. 16). The reduction in the fluctuation level is more pronounced at the outer region. The change of the fluctuations is also clear by looking at the potential and density fluctuations contours (Fig. 17). We can see a reduction in the level and also on the characteristic scales of the fluctuations.

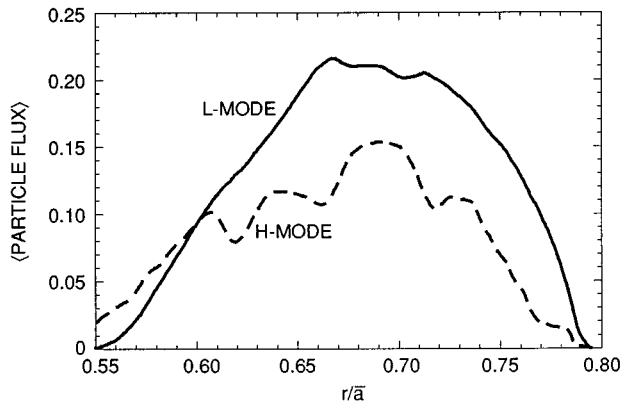


FIG. 15. Radial profile of the averaged particle flux in the L- and the H-mode states.

In the H-mode phase, there is also an increase in the averaged edge density pedestal. The combination of flux reduction and increased density gradient leads to a 35% improvement in the radial-averaged effective diffusivity (Fig. 18).

The confinement improvement is relatively low, even in the limit of negligible poloidal flow damping. This is the consequence of the structure of the Reynolds stress for resistive interchange turbulence. The Reynolds stress has two terms.²¹ One is proportional to the averaged poloidal flow velocity, and the second one is proportional to its second derivative,

$$-\frac{1}{r^2} \frac{\partial}{\partial r} (r^2 \langle \tilde{V}_r \tilde{V}_\theta \rangle) |_{x=0} = \langle \tilde{V}_r \tilde{U} \rangle |_{x=0} = \alpha \langle V_\theta \rangle + \beta \frac{d^2 \langle V_\theta \rangle}{dr^2}, \quad (17)$$

where α and β are positive coefficients depending on the fluctuation amplitude and plasma parameters. The α term leads to a dynamo instability and the generation of sheared flow. The β term is an effective turbulent viscosity that damps poloidal flow. In all these calculations, the β term quickly overtakes the α term, leading to a saturation of the

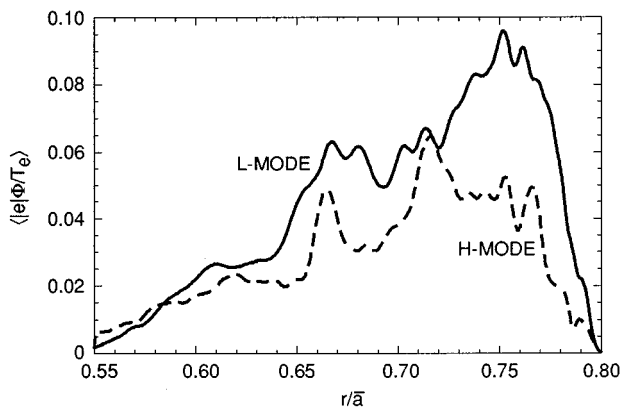


FIG. 16. Radial profile of the rms electrostatic potential fluctuations in the L- and the H-mode states.

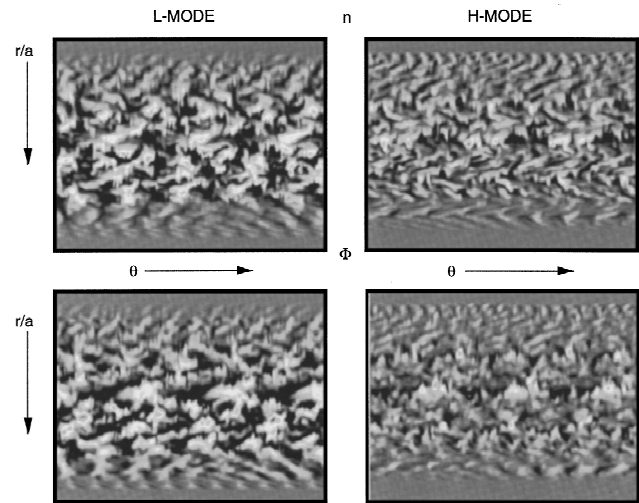


FIG. 17. Contours of the electrostatic potential and density fluctuations in the L- and H-mode phases.

poloidal flow before the poloidal flow shear is large enough to suppress the fluctuations, and only a partial reduction of the fluctuations is achieved.

The radial correlation length of the potential fluctuations remains nearly unchanged in the H-mode regime, while the density fluctuations radial correlation length is reduced. The radial averaged value of the radial correlation length of the electrostatic potential fluctuations is $\Delta_r = 0.0075 \pm 0.004a$ and for the density fluctuations $\Delta_r = 0.006 \pm 0.004a$. Those changes are consistent with the small reduction on the diffusivities. There is also little change on the poloidal wave number spectrum. There is no change in the spectral decay index. The mean value of the poloidal mode number averaged in time and radius is 15 in the L-mode phase and changes to 18 in the H-mode phase. The decorrelation time is also reduced in the H-mode phase. Of course, to determine the proper decorrelation time it has to be calculated in the plasma rest frame. We find that a typical decorrelation time is $\tau_c \approx 1.0 \times 10^{-3} \tau_R$.

In these calculations, the transition is characterized by a sharp increase in the poloidal flow and poloidal flow shear (Fig. 19). In the H-mode state, the radial oscillations in the

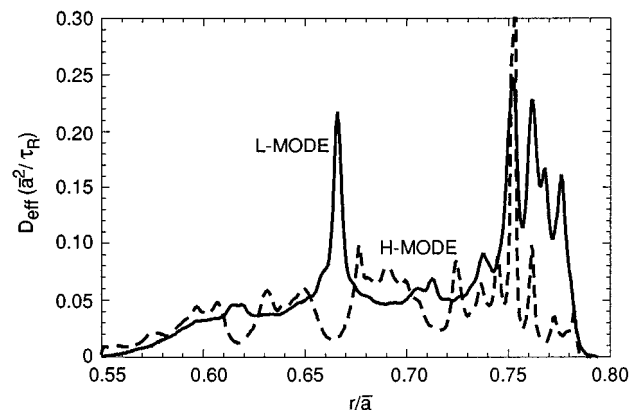


FIG. 18. Radial profile of the effective particle diffusivity in the L- and the H-mode states.

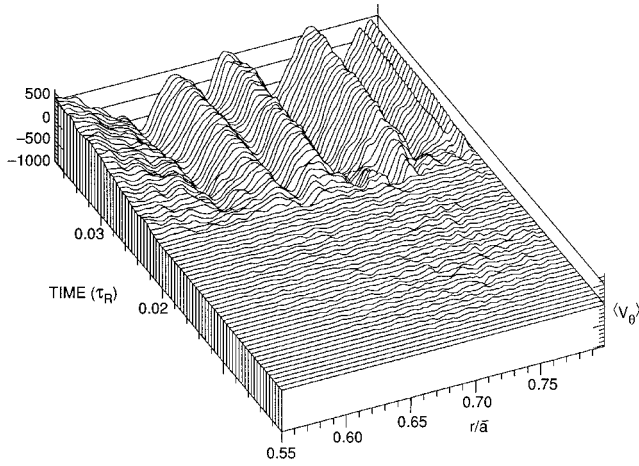


FIG. 19. Time evolution of the poloidal flow showing the fast increase at the transition.

poloidal flow profile are about a factor of 25 larger than before the transition (Fig. 20). Also, the scale length of the oscillations has changed. In the L mode, the radial structures are correlated with many of the low- n resonances surfaces ($n \leq 9$). The characteristic scale length of the poloidal flow, Δ_L , is of the order of the radial correlation length, which is basically the mode width. However, in the H mode, the radial structure of the flow is simpler and only correlates with a few of the very lowest- n resonant surfaces ($n \leq 3$ in this particular case). The characteristic scale length of the poloidal flow, Δ_H , is the distance between these surfaces, which is larger than the mode width. This distance is of the order of $\Delta_H \approx [n(n+1)q']^{-1}$, where n is the lowest resonant n number in the region considered. In the present calculations, this characteristic radial scale only varies by about 50%. For ATF parameters, this gives $0.9 \text{ cm} \leq \Delta_H \leq 1.7 \text{ cm}$.

There is a nonunique solution for the poloidal flow in the H-mode regime. In Fig. 21, we compare the radial profile of the flow from Fig. 20 with the result from another calculation with different initial conditions. We have also indicated in this figure the rational surfaces associated with the minima of the poloidal flow. We can see that these surfaces are differ-

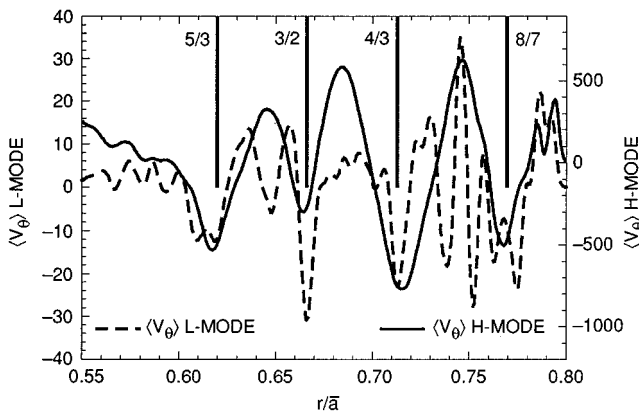


FIG. 20. Radial profile of poloidal flow in the L- and the H-mode states. The singular surfaces associated with the minima of the H-mode poloidal flow profile are indicated with vertical bars.

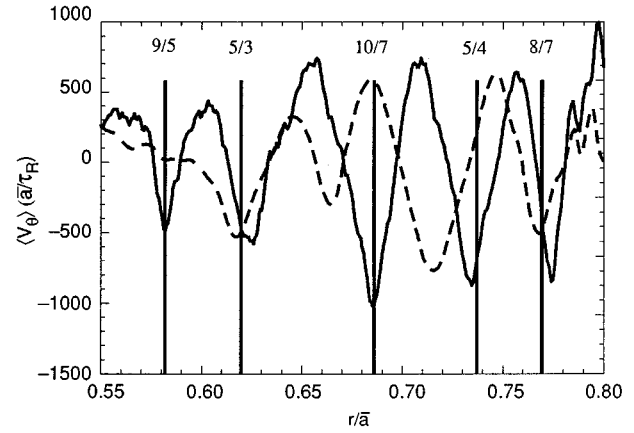


FIG. 21. A comparison of the radial profile of poloidal flow in the H-mode state for two calculations with different initial conditions. One profile corresponds to the same calculation as in Fig. 19. For the other calculation, the singular surfaces associated with the minima of the poloidal flow are indicated with vertical bars.

ent. However, the basic scale length of the flow is similar to the first case considered. In these calculations, the wave-like pattern of the poloidal flow is the result of lowering the poloidal flow damping over the whole radial extent. That is not what can be expected in the experiment. The poloidal flow damping has a radial dependence that is a function of collisionality. The region of the plasma in which the $E \times B$ flow would be significantly nonzero will probably be limited to the near-edge region. However, to determine that dependence from this type calculation would require the inclusion of sources and evolution over transport time scale.

The radial flow structure obtained in the three-dimensional (3-D) calculations is different from the results of single helicity 2-D calculations. In the single helicity case, the radial scale length of the poloidal flow is basically the mode width. This can be seen in Fig. 22, where we have plotted the poloidal flow from the 3-D results and compared it with the poloidal flow for two of the main single helicities.

A fluctuation reduction criterion that is commonly used in the analysis of experiments is a simplified version of the Biglari *et al.*, criterion²² in which the decorrelation time of the turbulence is taken to be the inverse of the maximum

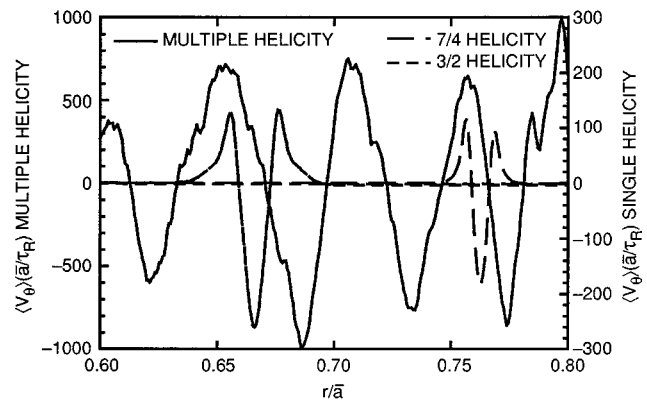


FIG. 22. Poloidal flow from the 3-D results and compared with the poloidal flow obtained from the 2-D single helicity calculation for two of the main helicities.

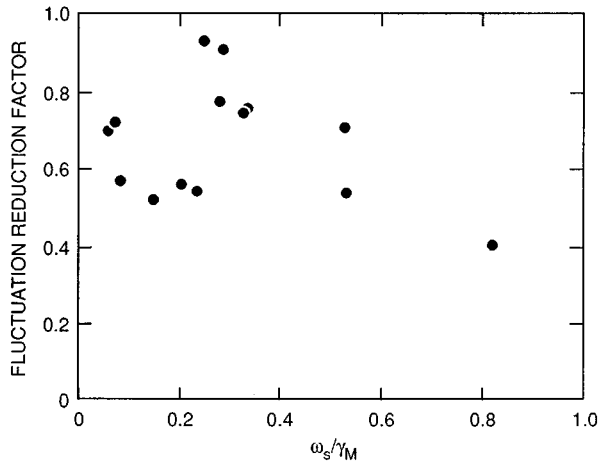


FIG. 23. Fluctuation reduction factor versus the normalized shearing rate for all resonant surfaces, with lowest- n values less than or equal to 7.

linear growth rate. We can compare this criterion with our results. To do so, we have chosen the radial position of the lowest q resonant modes with $n \leq 7$ and calculated the maximum linear growth rate, γ_M , for these helicities. The shearing rate, ω_s , at the corresponding resonant surfaces has been determined by

$$\omega_s = \frac{\Delta_r}{\Delta_\theta} \frac{d\langle V_\theta \rangle}{dr}. \quad (18)$$

In Fig. 23, we compare the fluctuation reduction factor (ratio of the local fluctuation level in the H mode to the fluctuation level in the L mode) to the normalized shearing rate, ω_s/γ_M . Although there is a qualitative correlation, the quantitative agreement is poor. This result should caution us on the use of this oversimplifying form of the fluctuation reduction criterion.

VI. CONCLUSIONS

Resistive interchange turbulence has been used to model the outer one-third of the ECH plasmas in the ATF device. This model reproduces some of the features of the observed edge turbulence: (1) the fluctuation levels and (2) the radial correlation lengths are consistent with the measurement by fluctuation diagnostics. However, the associated transport is somewhat lower. This is a consequence of the nearly adiabatic character of the fluctuations. The inclusion of trapped-electron instabilities²³ could be necessary for a more complete modeling of the outer region of the plasma.

Using this same turbulence model, we have investigated the possibility of transitions to a high-confinement mode. The physics mechanism for the transition is the creation of a $E \times B$ shear flow barrier. Because of the high toroidal flow damping in stellarators and the low ion temperature of the ECH plasmas, the only significant contribution to the electric field shear is the poloidal velocity shear. In the framework of this model, our calculations show the following.

- (1) When the poloidal flow shear is allowed to grow, there is a transition to a high-confinement regime with reduction of the fluctuation level mostly at the outer edge region.

- (2) The confinement improvement is relatively low, about 30%, even in the limit of negligible collisional flow damping. The effective turbulent viscosity component of the Reynolds stress quickly overcomes the dynamo instability component [Eq. (17)], causing the saturation of the poloidal flow.
- (3) In the H mode, it has been found that the characteristic radial scale length of the poloidal flow in the 3-D calculations is different from the single helicity results. In the latter case, the basic scale length of the flow is the radial correlation length of the fluctuations, while for the H-mode solution the basic scale is the separation between the lowest- n resonant surfaces. This scale length has not yet been considered in the analysis of edge temperature pedestals.
- (4) The oversimplified version of the Biglari–Diamond–Terry criterion,²² comparing the shearing rate to the linear growth rate, is not quantitatively consistent with the results of the numerical calculation. Therefore, caution should be taken in using this form of the criterion for experimental tests of the shear flow suppression mechanism.

The possibilities of accessing a high-confinement H mode in stellarator ECH discharges are very limited. Neither toroidal flow nor ∇p_i effects can contribute to the buildup and sustainment of the edge transport barrier, and the edge collisionality is too high to have a jump between roots of the electric field. This calculation shows that the poloidal shear flow cannot by itself provide a high enough confinement improvement. Therefore, some level of ion heating is probably required. We have to extend the present calculations to investigate this possibility and to assess the following.

- (1) For a realistic neoclassical viscosity, the effect of ∇p_i and V_θ shear combined in creating an edge transport barrier.
- (2) The change in the radial scale length of the electric field when ∇p_i is included in the calculation.

ACKNOWLEDGMENTS

We thank Carlos Hidalgo and G. Hanson for providing us with the fluctuation data from the ATF. We gratefully acknowledge invaluable help from the NERSC staff, in particular, Bruce Curtis for optimization of our codes to the C-90, and Tim Pierce, Greg Tomaschke, and Emily Yim for parallel ports and algorithm development for the T3D. We gratefully acknowledge pointed, but nevertheless constructive, comments and suggestions by P. H. Diamond.

This work has been performed as part of the U.S. Department of Energy's Numerical Tokamak Grand Challenge Project under Contract No. DE-AC05-84OR21400 with Lockheed Martin Energy Systems, Inc., and sponsored in part by the Direccion General de Investigación Científico y Técnica (Spain) under Project No. PB93-0231-CO2-01.

¹F. Wagner, J. Baldzuhn, R. Brakel, R. Burhenn, and V. Erckmann, *Plasmas Phys. Controlled Fusion* **36**, A61 (1994).

²K. Toi, T. Morisaki, S. Sakakibara, A. Ejiri, and H. Yamada, in *Proceedings of the 15th International Conference on Plasma Physics and Con-*

- trolled Nuclear Fusion Research* (International Atomic Energy Agency Vienna, 1995), Vol. 2, p. 331.
- ³B. A. Carreras, V. E. Lynch, and L. Garcia, *Phys. Fluids B* **3**, 1438 (1991).
- ⁴P. H. Diamond and Y. B. Kim, *Phys. Fluids B* **3**, 1626 (1991).
- ⁵B. A. Carreras, G. Griger, J. H. Harris, J. L. Johnson, J. F. Lyon, O. Motojima, F. Rau, H. Renner, J. A. Rome, K. Uo, M. Wakatani, and H. Wobig, *Nucl. Fusion* **28**, 1613 (1988).
- ⁶H. P. Furth, J. Killeen, and M. N. Rosenbluth, *Phys. Fluids* **6**, 459 (1963).
- ⁷B. A. Carreras, L. Garcia, and P. H. Diamond, *Phys. Fluids* **30**, 1388 (1987).
- ⁸H. Sugama and M. Wakatani, *J. Phys. Soc. Jpn.* **57**, 2010 (1988).
- ⁹G. S. Lee, B. A. Carreras, and L. Garcia, *Phys. Fluids B* **1**, 119 (1989).
- ¹⁰S. Hamaguchi, *Phys. Fluids B* **1**, 1416 (1989).
- ¹¹G. R. Hanson, J. H. Harris, J. B. Wilgen, C. E. Thomas, S. C. Aceto, L. R. Baylor, J. D. Bell, B. Brañas, J. L. Dunlap, A. C. England, C. Hidalgo, M. Murakami, D. A. Rasmussen, J. Sanchez, J. G. Schwelberger, T. Uckan, and J. J. Zielinski, *Nucl. Fusion* **32**, 1593 (1992).
- ¹²C. Hidalgo, J. H. Harris, T. Uckan, G. R. Hanson, J. D. Bell, M. A. Meir, C. P. Ritz, and A. J. Wootton, *Nucl. Fusion* **33**, 146 (1993).
- ¹³J. M. Greene and J. L. Johnson, *Phys. Fluids* **4**, 485 (1961).
- ¹⁴K. C. Shaing, *Phys. Fluids B* **5**, 3841 (1993).
- ¹⁵L. M. Kovrizhnykh, *Sov. Phys. JETP* **29**, 475 (1969).
- ¹⁶J. F. Lyon, B. A. Carreras, K. K. Chiple, M. J. Cole, J. H. Harris, T. C. Jernigan, R. L. Johnson, V. E. Lynch, B. E. Nelson, J. A. Rome, J. Sheffield, and P. B. Thompson, *Fusion Technol.* **8**, 179 (1986).
- ¹⁷L. Garcia, H. R. Hicks, B. A. Carreras, L. A. Charlton, and J. A. Holmes, *J. Comput. Phys.* **65**, 253 (1986).
- ¹⁸H. Sugama and W. Horton, *Comments Plasma Phys. Control. Fusion* **17**, 277 (1996).
- ¹⁹C. Hidalgo, J. H. Harris, T. Uckan, J. D. Bell, B. A. Carreras, J. L. Dunlap, G. R. Dyer, C. P. Ritz, A. J. Wootton, M. A. Meir, T. L. Rhodes, and K. Carter, *Nucl. Fusion* **31**, 1471 (1991).
- ²⁰For a general reference for CHS, see K. Matsuoka, S. Kubo, M. Hosokawa, Y. Takita, S. Okamura, N. Noda, H. Yamada, H. Iguchi, K. Masai, S. Morita, K. Ida, H. Idei, C. Takahashi, K. Nishimura, T. Shoji, H. Sanuki, M. Fujiwara, Y. Abe, T. Amano, A. Ando, T. Aoki, D.-G. Bi, J. Fugita, S. Hidekuma, T. Kamimura, O. Kaneko, T. Kawamoto, A. Mohri, A. Nishizawa, S. Tanahashi, J. Todoroki, K. Tsuzuki, K. Yamazaki, in *Proceedings of the 15th International Conference on Plasma Physics and Controlled Nuclear Fusion* (IAEA, Vienna, 1989), Vol. 2, P. 411; for W7-AS, S. Sattler, H. J. Hartfuss, and the W7-AS team, *Phys. Rev. Lett.* **72**, 653 (1994).
- ²¹B. A. Carreras, V. E. Lynch, L. Garcia, and P. H. Diamond, *Phys. Plasmas* **2**, 2744 (1995).
- ²²H. Biglari, P. H. Diamond, and P. W. Terry, *Phys. Fluids B* **2**, 1 (1990).
- ²³N. Dominguez, B. A. Carreras, V. E. Lynch, and P. H. Diamond, *Phys. Fluids B* **4**, 2894 (1992).